Control of a PMSM Using the Rotor-Side Converter of a Doubly-fed Induction Generator for Hybrid-Electric Propulsion

Md Abid Hossain, *Member, IEEE*, and Marc Bodson, *Fellow, IEEE*

***Abstract*— A traditional hybrid electric propulsion system requires two full-rated converters to convert the electric power from the generator to motor. This paper proposes a method to control the speed of a permanent-magnet synchronous motor (PMSM) receiving power from a doubly-fed induction generator (DFIG) and using the generator's rotor-side converter. This technique can reduce the size and number of converters in a hybrid-electric propulsion system. An integrated model of the system is developed, which is then used to derive the control algorithm. The presentation is simplified by using a complex representation of the dynamic system and of the control law. A voltage and a current command mode are considered and limiting is incorporated to ensure the satisfaction of current constraints. Experimental data show excellent tracking performance of speed references and improved recovery from large load disturbances compared to operation using a synchronous generator. A storage element provides or recovers excess power through the rotor-side converter of the DFIG.**

***Index Terms*— Permanent-magnet synchronous motors, doubly-fed induction generators, hybrid-electric propulsion, variable speed drives, mechanical power transmission.**

I. Introduction

Hybrid electric (land) vehicles are attractive due to improved fuel economy, reduced pollution, and lower noise. Hybrid-electric propulsion solutions are being investigated for aircraft and present similar advantages [1]. The hybrid-electric technology can expand the design space, and systems integration can provide additional benefits for larger systems [2]. Fig. 1 shows a series-connected topology as may be used in ships [3] and aircrafts [4]. A generator produces AC power that is converted to DC and then back to AC to drive a motor, which will be assumed to be a PMSM. A DC/DC converter connects a storage system to the DC bus. The topology is used for hybrid-electric vehicles (HEVs) [5], but with a higher relative storage capability than may be feasible for aircraft.

A drawback of the solution of Fig. 1 is that converters rated for the maximum power are needed, implying a significant weight contribution of the devices and their cooling systems. Energy losses are significant, especially at high load conditions [6]. An alternative option consists of connecting the generator directly to the PMSM. If a synchronous generator is used, this option eliminates the need for the DC/AC converters altogether, but also removes the flexibility of controlling the speed of the motor independently of the generator. Further, the solution is risky, due to the possibility of loss of synchronism.

This paper considers the alternative concept shown in Fig. 2, where a doubly-fed induction generator with a rotor-side DC/AC converter drives a PMSM. A related concept was proposed in [7], where the PMSM was replaced by a doubly-fed induction motor. The rotor-side converter of the generator increases the controllability of the system compared to a synchronous generator, and enables operation at non-synchronous speeds. The DFIG presents the same advantages as those that have made the machine advantageous for wind power generation [8]. If the speed is limited to some interval around the synchronous speed, a single DC/AC converter rated at a fraction of the full power replaces the two full-rated converters of Fig. 1. In wind power, a 30% speed range is typical, and translates into a 30% converter rating (approximately). Further, most of the power is transmitted directly from the stator of one machine to the other, reducing significantly the conversion losses. The total weight of the converters and associated cooling systems can therefore be lowered considerably for an airborne multi-MW system.

Control methods for PMSMs using three-phase inverters are widely available, but the scheme of Fig. 2 brings up a new question: is it possible to control a PMSM *through* a DFIG, i.e., using the rotor-side converter of the DFIG? Such a possibility appears likely but note that the problem is far from trivial. In particular, it is impossible to apply DC currents to the motor. Also, it is very different to control a DFIG connected to an infinite grid that specifies the stator voltages and a DFIG connected to a motor that generates a variable back-emf. Further, the dynamics of the generator become part of the system to be controlled and are closely coupled to those of the motor, with currents in the two machines equal but of opposite sign.

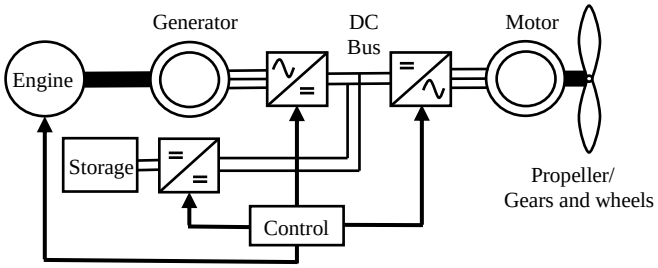

Fig. 1. Block diagram of a conventional hybrid-electric propulsion technique.

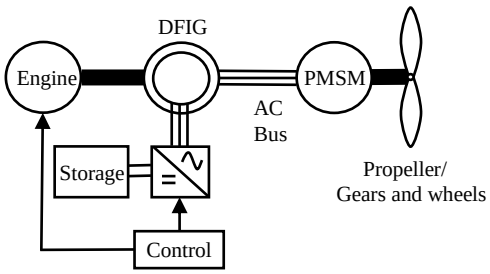

Fig. 2. Proposed control technique using a DFIG and a PMSM.

This paper is submitted for review on March 20, 2021.

M. A. Hossain is with the Electrical and Computer Engineering Department, University of Utah, Salt Lake City, UT 84112, USA (e-mail: mdabid.hossain@utah.edu).

M. Bodson is with the Electrical and Computer Engineering Department, University of Utah, Salt Lake City, UT 84112, USA (e-mail: marc.bodson@utah.edu).

Although a drawback of the doubly-fed induction machine (DFIM) is the need for slip rings, research work on the brushless DFIM (BDFIM) aims to resolve this issue with various rotor configurations having been proposed such as cage rotors [9], reluctance rotors [10], wound rotors [11], hybrid rotors [12], and dual-stator BDFIM [13]. These machines do not require slip rings and the dynamics of some of them are identical to those of the DFIM. In other cases, the dynamics can be approximated by those of a DFIM.

The literature related to HEV/EV and hybrid ship applications includes papers on optimization with energy management [14,15] (HEV/EVs) [16,17] (hybrid ships), converter design [18,19] (HEV/EVs) [20,21] (hybrid ships), and different kinds of motor constructions [22,23]. For hybrid aircrafts, distributed propulsion [24] and flexible wings [25] have also been proposed in combination with hybrid electric propulsion to further reduce the fuel burn. Few studies consider the control problem for motor/generator sets. A study proposes an integrated control system for a DFIM and a wound rotor synchronous generator [26]. The paper studies the system with the Port Controlled Hamiltonian model and Bond graph model in the complex coordinates. No experimental results are reported. [4] proposes a similar system as Fig. 2, but with doubly-fed induction machines for the generator and the motor.

The paper contains six sections. After this introduction, the second section uses the models of the DFIG and PMSM in the complex domain to obtain an integrated model of the combined system. The third section presents the proposed control method. The fourth section provides experimental results and demonstrates the performance of the controller under different conditions. The proposed scheme is shown to improve the recovery from large load disturbances compared to a WFSG. The fourth section also discusses possible techniques for the management of the battery's stored energy. The fifth section gives directions for future research, and the sixth section summarizes the conclusions of the paper.

II. Complex Model of a Motor/Generator Set

A. Complex Representation

The paper uses compact representations of the machines using complex variables. For a three-phase machine with line-neutral voltages v_{SA}, v_{SB} and v_{SC}, a complex voltage v_S is defined as

$$v_S = \sqrt{\frac{2}{3}}\left(v_{SA} + v_{SB}\, e^{j\frac{2\pi}{3}} + v_{SC}\, e^{-j\frac{2\pi}{3}}\right) e^{-j\theta_S} \tag{1}$$

where θ_S is an angle to be defined so that the voltage v_S is constant in steady-state. Compared to standard models using *dq* transformations, the approach corresponds to the grouping of the *dq* variables into a single complex variable using

$$v_S = v_d + jv_q \tag{2}$$

The same transformation (1) is applied to the line currents to give the complex current i_S. The scaling factor of $\sqrt{2/3}$ is such that power computed in the three-phase variables is identical to power computed in the *dq* variables. The machines are assumed to be Y-connected, or represented as equivalent Y-connected machines.

B. Model of the PMSM

Consider a three-phase PMSM and let the mechanical angle θ be the angle between the direction of the permanent magnet and phase A of the stator. Then, the angle of the reference frame is set to $\theta_S = n_P\theta$, where n_P is the number of pole pairs of the motor. With these definitions, the standard model of the PMSM motor is

$$(sL_M + Z_M)i_S = v_S - jK\omega \tag{3}$$

with the torque

$$\tau_M = K\,\mathrm{Im}(i_S) \tag{4}$$

In the equations, s is the Laplace variable, $\omega = d\theta/dt$ is the mechanical speed of the motor, Im refers to the imaginary part, and

$$Z_M = R_M + j\omega_S L_M \tag{5}$$

where $\omega_S = n_P\omega$ is the electrical angular frequency of the reference frame, which becomes the frequency of the stator voltages and currents in steady-state. The parameters of the motor are R_M and L_M, the resistance and inductance of the motor windings, and K, the torque constant of the motor.

C. Model of the Doubly-fed Induction Generator

When a DFIG is connected to a PMSM motor, as shown in Fig. 2, the voltages on the windings of the DFIG are the same as the voltages on the windings of the PMSM motor. The currents are also identical, but with reversed signs. In the complex domain, the stator voltages and currents of the DFIG are v_S and $-i_S$, respectively. If the voltages applied to the rotor windings are denoted v_{RX}, v_{RY}, v_{RZ} the complex transformation for the rotor voltages is defined through

$$v_R = \sqrt{\frac{2}{3}}\left(v_{RX} + v_{RY}\, e^{j\frac{2\pi}{3}} + v_{RZ}\, e^{-j\frac{2\pi}{3}}\right) e^{-j\theta_R} \tag{6}$$

where θ_R is the electrical angle for the rotor windings. θ_R is given by

$$\theta_R = \theta_S - n_{PG}\theta_G \tag{7}$$

where θ_G is the mechanical position of the rotor of the DFIG (the angle between winding *X* of the rotor and winding *A* of the stator) and n_{PG} is the number of pole pairs of the generator. The transformation (6) is also applied to the rotor currents.

The standard model of a DFIG expressed in the complex coordinates is [4] [27]

$$\begin{aligned} -(sL_S + Z_S)\, i_S + (sM + j\omega_S M)\, i_R &= v_S \\ (sL_R + Z_R)\, i_R - (sM + j\omega_R M)\, i_S &= v_R \end{aligned} \tag{8}$$

where

$$Z_S = R_S + j\omega_S L_S\,,\; Z_R = R_R + j\omega_R L_R \tag{9}$$

and

$$\omega_R = \omega_S - n_{PG}\omega_G \tag{10}$$

In the equations, $\omega_G = d\theta_G/dt$ is the mechanical speed of the generator. In steady-state, $\omega_R = d\theta_R/dt$ becomes the electrical frequency of the rotor voltages and currents. The parameters of the model are R_S and R_R, the stator and rotor winding resistances, L_S and L_R, the stator and rotor winding inductances, and M, the mutual inductance between stator and rotor windings.

D. Integrated Model of the Motor/Generator Set

By subtracting the first equation of (8) from (3), the following model of the motor/generator set as shown in Fig. 2 is obtained

$$\begin{aligned}(sL_T + Z_T)\, i_S - (sM + j\omega_S M) i_R &= -jK\omega \\ (sL_R + Z_R)\, i_R - (sM + j\omega_R M) i_S &= v_R\end{aligned} \tag{11}$$

where $L_T = L_S + L_M$ and $Z_T = Z_S + Z_M$. The control problem consists of determining the voltage v_R such that the torque τ_M defined in (4) follows a torque command $\tau_{M,COM}$. The torque command can then be used to control the speed of the motor. Note that the d-axis of the reference frame is aligned with the permanent magnet of the PMSM, so that the control algorithm to be developed implements a form of field-oriented control for the PMSM that accounts for the coupled dynamics of both machines.

III. Control Algorithm

A control system to regulate the speed of the motor is shown in Fig. 3. In the figure, ω_{REF} is the reference speed of the motor, $\tau_{M,COM}$ is a torque command, $\tau_{M,LIM}$ is a torque command limited to satisfy current constraints, $i_{R,COM}$ is a rotor current command, and $i_{R,MAX}$, $i_{S,MAX}$ are limits on the magnitudes of the complex rotor and stator currents. These limits may originate from the ratings of the converters and of the two machines. The elements of the control system are reviewed in the following sections.

A. Speed Control

The torque command for the motor, $\tau_{M,COM}$, is derived from a reference speed, ω_{REF}, and from the actual speed of the motor, ω, using a proportional-integral controller

$$\tau_{M,COM} = K_P(\omega_{REF} - \omega) + K_I \int (\omega_{REF} - \omega) dt \tag{12}$$

where K_P and K_I are proportional and integral gains. Assuming that the torque of the motor follows the command, the speed response is determined by

$$J\frac{d\omega}{dt} = \tau_M - \tau_L \cong \tau_{M,COM} - \tau_L \tag{13}$$

where J is the inertia of the motor plus load, and τ_L is the non-inertial part of the load torque. The load torque is treated as a disturbance so that the closed-loop transfer function is given by

$$\frac{\omega}{\omega_{REF}} = \frac{K_P s + K_I}{Js^2 + K_P s + K_I} \tag{14}$$

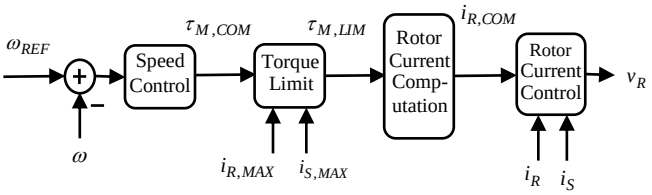

Fig. 3. Block diagram of the control system.

The closed-loop poles of (14) are the roots of

$$Js^2 + K_P s + K_I = 0 \tag{15}$$

and can be set at some desired value α_D by letting $K_P = 2\alpha_D J$ and $K_I = \alpha_D^2 J$. In the implementation of (12), $K_P(\omega_{REF} - \omega)$ was replaced by $K_P(K_F\omega_{REF} - \omega)$ with $K_F = 2/3$ to improve the response by moving the zero of the closed-loop transfer function further into the left half-plane (see [27] for more details). In aircraft applications, the load torque is mostly due to aerodynamic friction and is proportional to the rotational speed squared. A predicted value of this torque could be added in the torque command based on the reference speed.

B. Torque Limit

The stator current command is based on (4) and quadrature control (zero current along the *d* axis), so that

$$i_{S,COM} = ji_{Sq,COM} \text{ with } i_{Sq,COM} = \tau_{M,COM}/K \tag{16}$$

Then, the rotor current command is computed using the steady-state response obtained by letting $s = 0$ in (11), so that

$$Z_T i_S - j\omega_S M i_R = -jK\omega \tag{17}$$

The following rotor current command is obtained

$$i_{R,COM} = \frac{K\omega}{\omega_S M} + \frac{R_T}{\omega_S M} i_{Sq,COM} + \frac{L_T}{M} ji_{Sq,COM} \tag{18}$$

The torque command is then limited to satisfy constraints on the stator and rotor currents. From (16), the limit associated with the stator current is straightforward, with

$$\tau_{M,MAX1} = Ki_{S,MAX} \tag{19}$$

where $\tau_{M,MAX1}$ is the torque limit due to the maximum stator current, $i_{S,MAX}$. (18) implies that $|i_{R,COM}| \le i_{R,MAX}$, where $i_{R,MAX}$ is the limit on the rotor current, if and only if

$$a_1 i_{Sq,COM}^2 + 2a_2 i_{Sq,COM} + a_3 \le 0 \tag{20}$$

where

$$a_1 = \left(\frac{R_S + R_M}{\omega_S M}\right)^2 + \left(\frac{L_S + L_M}{M}\right)^2$$
$$a_2 = \frac{K\omega}{\omega_S M}\left(\frac{R_S + R_M}{\omega_S M}\right) \quad (21)$$
$$a_3 = \frac{K^2\omega^2}{\omega_S^2 M^2} - i_{R,MAX}^2$$

Note that $a_1 > 0$ and $a_2 > 0$ for $\omega > 0$. The limit $i_{R,MAX}$ on the rotor current must be large enough so that $a_3 < 0$, or there can be no solution. Then, the maximum torque $\tau_{M,MAX\,2}$ considering the rotor current limit is deduced to be

$$\tau_{M,MAX\,2} = K\frac{-a_2 + \sqrt{a_2^2 - a_1 a_2}}{a_1} \quad (22)$$

The output of the torque limiting block, $\tau_{M,LIM}$, is the torque command $\tau_{M,COM}$ limited to the values given by (19) and (22). If a torque limit is reached, an anti-windup technique also needs to be applied in the PI controller for velocity control.

C. Rotor Current Computation

The rotor current command is calculated using (16) and (18) with the torque limited to the maximum value, so that

$$i_{S,COM} = j\frac{\tau_{M,LIM}}{K}, i_{R,COM} = \frac{jK\omega + Z_T i_{S,COM}}{j\omega_S M} \quad (23)$$

D. Rotor Current Control

Two methods are developed for the control of the complex rotor current. In the first method (voltage command mode), an open-loop control algorithm calculates the rotor voltages based on the steady-state model. In the second method (current command mode), a closed-loop control algorithm actively regulates the currents.

1) Voltage Command Mode

In this method, the rotor voltage is determined based on the model (11) in steady-state, so that

$$v_{R,COM} = Z_R i_{R,COM} - j\omega_R M i_{S,COM} \quad (24)$$

The main drawback of this open-loop technique is that the rotor current is not actively regulated, and tracking may not be precise due to modeling uncertainties.

2) Current Command Mode

The current command mode is based on the method presented in [27], which was derived from the control scheme of [28] for induction motors. The dynamic model in (11) can be expressed as

$$\begin{bmatrix} L_T & -M \\ -M & L_R \end{bmatrix}\begin{bmatrix} \frac{di_S}{dt} \\ \frac{di_R}{dt} \end{bmatrix} = \begin{bmatrix} -u_S \\ -u_R + v_R \end{bmatrix} \quad (25)$$

where

$$u_S = Z_T i_S - j\omega_S M i_R + jK\omega$$
$$u_R = Z_R i_R - j\omega_R M i_S \quad (26)$$

From (25)

$$\left(L_R - \frac{M^2}{L_T}\right)\frac{di_R}{dt} = -\frac{M}{L_T}u_S - u_R + v_R \quad (27)$$

and the following algorithm is deduced

$$v_R = u_R + \frac{M}{L_T}u_S + \left(L_R - \frac{M^2}{L_T}\right)$$
$$\left(K_{PC}(i_{R,COM} - i_R) + K_{IC}\int(i_{R,COM} - i_R)dt\right) \quad (28)$$

where K_{PC} and K_{IC} are proportional and integral gains of the current control loop. Note that (28) represents two PI controllers in the *dq*-domain. In the Laplace domain, (27) with (28) imply that

$$si_R = \left(K_{PC} + \frac{K_{IC}}{s}\right)\left(i_{R,COM} - i_R\right) \quad (29)$$

so that the response of the current control loop satisfies

$$i_R = \frac{K_{PC}s + K_{IC}}{s^2 + K_{PC}s + K_{IC}} i_{R,COM} \quad (30)$$

A possible design option consists in setting the two poles of the current loop at the desired value $s = -a_{DC}$. The placement of the poles is obtained for $K_{PC} = 2a_{DC}$ and $K_{IC} = a_{DC}^2$. The choice of a_{DC} can be based on the inverse of the desired time constant or the desired bandwidth of the current loop in rad/s. Noise in the measurements and neglected dynamics limit the maximum value of the parameter a_{DC}.

The algorithm proposed here constitutes only one possible option based on the model of the integrated motor/generator set. Other possibilities include the use of the model (25) for the joint regulation of the stator and rotor currents.

IV. Experiments

A. Experimental Setup

Fig. 4 shows the main components and connections for the experimental setup. A dSPACE DS 1104 (DAC system) served as an interface between the real-world components and the control system programmed in Matlab/Simulink. A Hirel inverter board, controlled by the DAC system, included two converters that provided the output voltages v_{DC} and v_R to the brush DC motor driving the generator and to the rotor windings of the DFIG. Current sensors on the board sensed the currents flowing through the converters. The DC motor acted as the prime mover and ran at some pre-specified profile to vary the speed of the DFIG without precise speed regulation. Another brush DC motor, mechanically coupled to the PMSM motor, served as a load. The load torque was modified using a resistor R_{Load} connected to the armature. The resistor was either connected or

disconnected through a separate command. The DC motors connected to the DFIG and the PMSM motor had encoders to measure the positions and the speeds of the generator and the motor. A dual current sensor, connected in series between the stator windings of the two machines, sensed the stator current i_S (more specifically, two of the physical currents, from which the complex current was computed).

Table 1 shows the parameters of the two machines. The DFIG is rated at 30 V and 4000 rpm, while the PMSM is rated at 36 V and 4000 rpm. Other values used in the control algorithm are listed in Table 2. Note that the maximum complex rotor current magnitude is $\sqrt{3/2}$ times the maximum peak line current with the transformation used in the paper. The limit on the stator current did not need to be applied in this testbed.

TABLE I
LIST AND VALUES OF THE MACHINE PARAMETERS

Symbols	PARAMETERS	Values
R_S	DFIG stator resistance	0.66 Ω
R_R	DFIG rotor resistance	0.94 Ω
L_S	DFIG stator inductance	13.1 mH
L_R	DFIG rotor inductance	9.8 mH
M	DFIG mutual inductance	9.7 mH
n_{PG}	DFIG number of pole pairs	2
R_M	PMSM stator resistance	0.9 Ω
L_M	PMSM stator inductance	2.2 mH
n_P	PMSM number of pole pairs	2
J	PMSM motor inertia	6.35×10^{-5} kg m^2
K	PMSM torque constant	0.046 N m/A

TABLE II
LIST AND VALUES OF THE CONTROLLER PARAMETERS

Symbols	PARAMETERS	Values
a_D	Desired pole for the speed loop	50 rad/s
a_{DC}	Desired pole for the current loop	100 rad/s
$i_{R,MAX}$	Maximum rotor current	$\sqrt{3/2}$ 6 A
$i_{S,MAX}$	Maximum stator current	Not used
f_{SW}	Inverter switching frequency	10 kHz
f_S	Sampling frequency	2.5 kHz

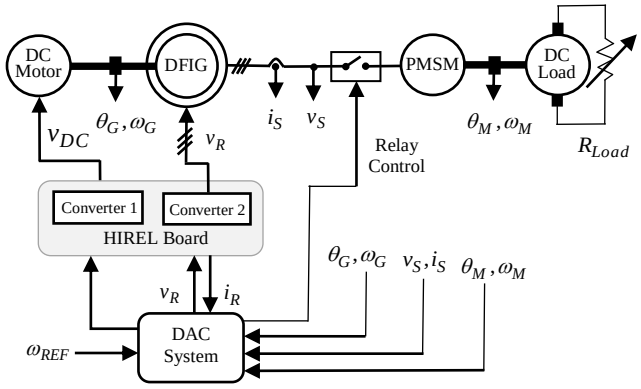

Fig. 4. The main components and connections of the experimental testbed.

B. Start-up Procedure and Estimation of the Encoder Offset

The models presented in section 2 assume that the positions of the rotors are such that the zero position corresponds to a specific alignment of the rotors. With incremental encoders, the measured positions are initialized at zero, resulting in an offset of the position measurement. In the case of the PMSM, a simple initialization method consists of applying DC currents at start-up. However, such a technique is not feasible in the testbed unless the machines are electrically disconnected, and a separate DC supply is used. To avoid this requirement, a start-up procedure was developed that includes the estimation of the encoder offsets for both machines.

First, a constant voltage is applied to the DC motor connected to the DFIG to bring the speed of the prime mover to about 1000 rpm. The PMSM motor is disconnected electrically at this time. A positive DC voltage is also applied to winding X of the rotor, with a zero-voltage applied to windings Y and Z of the DFIG. The stator voltages are measured, and the complex stator voltage is computed using $\theta_S = n_{PG}\theta_G$. The value is averaged over a short period of time to reduce the effect of noise. According to the DFIG model, i_R is real and $v_S = j\omega_S M$. Therefore, the offset of θ_G is the angle of v_S minus π/2, and divided by the number of pole pairs.

The PMSM motor is then connected to the DFIG. The synchronous speed of 1000 rpm is within a range where the PMSM accelerates in open-loop mode to the synchronous speed without excessive stator currents. The offset of the PMSM encoder is estimated using the position observer described in [29]. This technique determines the rotor position from the voltages and currents of the motor using a stationary reference frame $(\theta_S = 0)$.

After the estimation of the offset of the PMSM encoder, the control law is engaged. The positive rotor voltage applied to the DFIG is replaced by the voltage computed by the control law. The integrator of the PI controller for velocity is initialized to a value corresponding to the torque needed at 1000 rpm to reduce transients. Afterward, various velocity reference profiles are applied to test the performance of the control law.

C. Experimental Results

1) Tracking Performance

Results are presented for the current command mode. The responses in the voltage command mode are very similar, although small differences are observed when looking closely at the responses and are discussed later. Fig. 5 shows the speed reference and the speed of the motor, together with the speed of the generator. The speed reference ramps up to 1800 rpm after 1 s and climbs again to 3000 rpm at 2.5 s. Afterwards, the reference decreases along a similar pattern. The PMSM motor follows the reference closely. The voltage across the DC motor that serves as the prime mover is pre-planned so that the DFIG speed is not far from the reference. The generator operates in sub-synchronous mode, except before 1.5 s, between 3.125 s to 4.875 s, and after 6 s.

Fig. 6 shows the instantaneous powers delivered by the stator windings of the generator and absorbed by its rotor windings. The estimated ohmic losses were subtracted from the power variables as these losses are high in the small generator used in the experiments, and they obscure the fundamental behavior of the DFIG. The active powers rise during accelerations and with increasing motor speeds, due to friction losses. As the generator generally operates close to its synchronous speed, the rotor power is much smaller than the stator power. Fig. 7 shows the reactive power absorbed by the DFIG stator and rotor windings, respectively.

Fig. 8 shows the peak values of the stator and rotor currents. The variations of current are of comparable magnitude because the turns

ratio of the DFIG is close to one. The baseline rotor current is larger, due to the need to provide the reactive power required by both machines. Possibly, this current could be reduced by adding capacitors on the stator side.

Fig. 9 shows the peak voltages on the stator and rotor windings. As the DFIG is a small machine, the ohmic voltage drop is higher compared to a large machine. To remove this effect, the ohmic voltage drops from both sets of windings were removed from the data in Fig.

9. Then, the rotor voltage is significantly smaller than the stator voltage due to the limited range of slip under which the generator operates. This property indicates that a rotor-side converter with a reduced rating could be utilized, as in doubly-fed induction generators used for wind turbines.

Fig. 10 shows the commanded torque and the limit computed by the algorithm. Note that the large transient pulses on the torque could be reduced by slowing down the acceleration specified in the speed profile. Transients in power and current curves could also be reduced. Conversely, a reference with shorter ramping time pushes the torque to reach its limit.

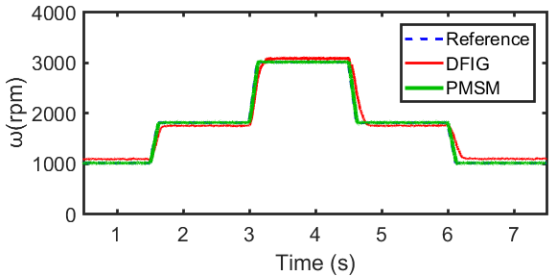

Fig. 5. Generator, motor, and reference speeds under current command.

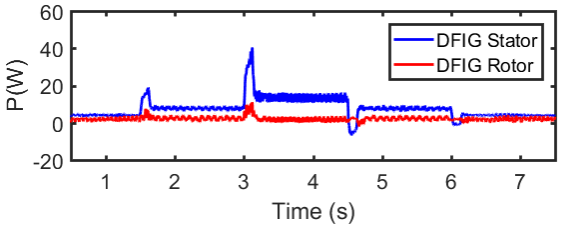

Fig. 6. Active power supplied by the stator windings and active power absorbed by the rotor windings of the DFIG, excluding ohmic losses.

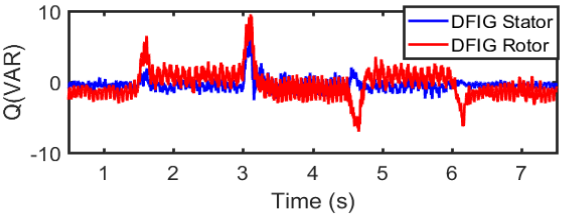

Fig. 7. Reactive power supplied by the stator windings and absorbed by the rotor windings of the DFIG.

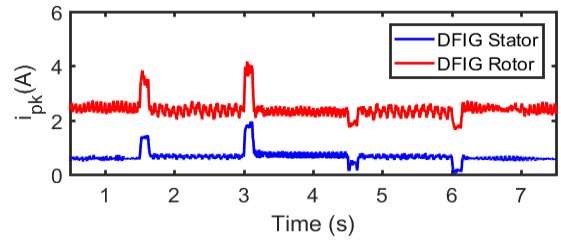

Fig. 8. Generator peak currents.

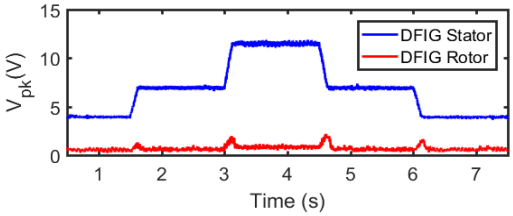

Fig. 9. Generator peak voltages excluding ohmic voltage drops.

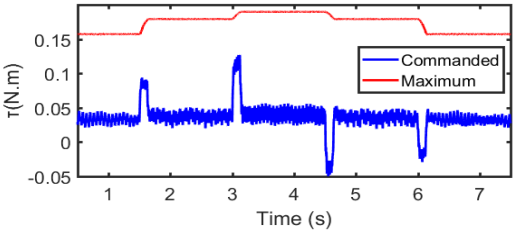

Fig. 10. Torque command with maximum torque limit under the current command mode.

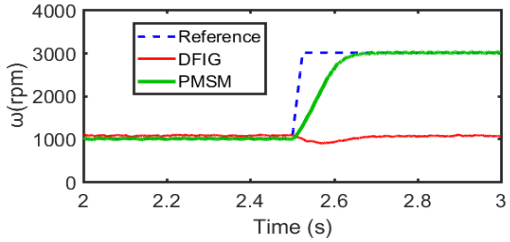

Fig. 11. Generator, motor, and reference speeds

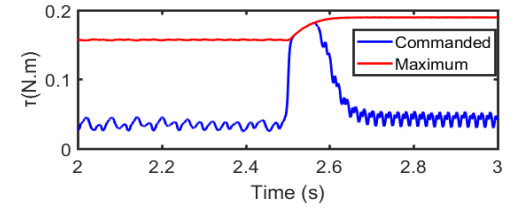

Fig. 12. Torque command with maximum torque

This case is considered in Figs. 11 and 12, where a high acceleration pushes the torque command to the limit imposed by the rotor current limit. Fig. 13 shows that the peak rotor winding current reaches but does not exceed the 6 A limit during the acceleration period.

2) Recovery from Large Load Disturbances

This section evaluates the ability of the control system to recover from large load disturbances. In aircraft propulsion, such disturbances could originate from a bird strike or a gust of wind. This test is the main motivation for considering a DFIG instead of a wound-field synchronous generator (WFSG). Indeed, a WFSG would run the risk of losing synchronism with the PMSM motor.

A DFIG with a DC current applied to the rotor is a synchronous generator. Using the DFIG to emulate a WFSG means that the same set-up could be used and that the DFIG and WFSG in the two experiments had comparable characteristics. The performance of the control system with the DFIG is then compared to the performance of the same system, but with a constant DC current applied to the rotor (with the positive on one line, and the negative on the other two lines tied together). To facilitate the comparison, the reference speed is set to be equal to the generator speed in the DFIG. Therefore, the conditions are similar to the WFSG operation, until the large load disturbance is applied.

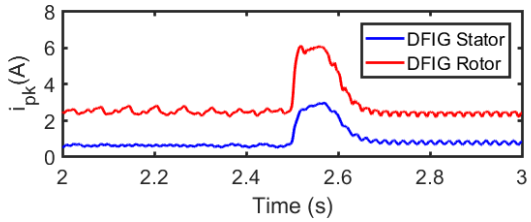

Fig. 13. Generator peak currents.

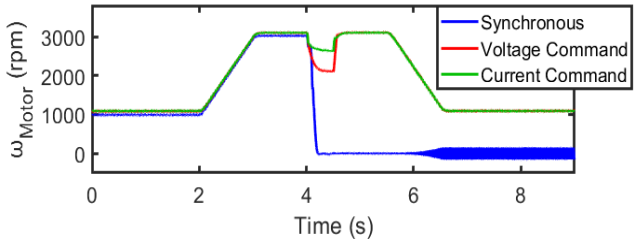

Fig. 14. Motor speeds for three controllers with large load disturbances.

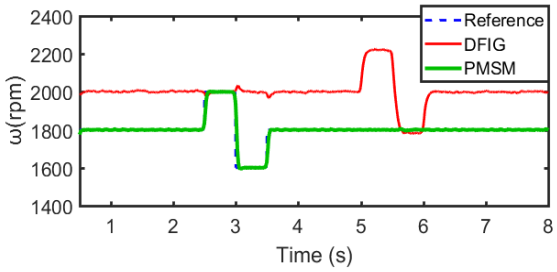

Fig. 15. Speeds of the motor and generator to illustrate rotor power conversion

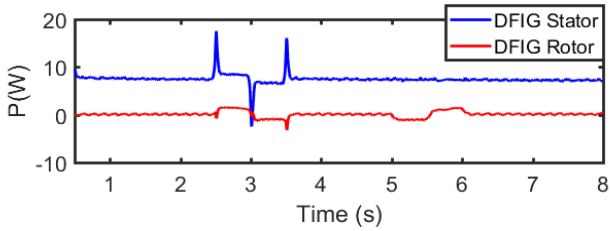

Fig. 16. Active powers to illustrate rotor power conversion.

The blue curve in Fig. 14 shows the speed of the motor when the DFIG is operated as a WFSG and a large load disturbance is applied. This load disturbance was obtained by connecting the resistance to the leads of the DC motor serving as a load during 0.05 s. Fig. 14 displays that the motor loses synchronism in WFSG mode. On the other hand, the red and green lines show that the motor remains synchronized under both voltage and current command modes with closed-loop DFIG control. A smaller speed drop is observed in the current command mode.

3) Management of Energy Storage

The concept of Fig. 2 raises the issue of the management of the stored energy and how the battery can be charged. Generally, doubly-fed induction generators producing power on their stator windings generate power on the rotor in super-synchronous operation and absorb power in sub-synchronous operation [30]. As a result, the stored energy can be used to boost the motor power through the rotor when accelerating. On the other hand, storage can be replenished by raising the speed of the prime mover speed while cruising.

To illustrate these properties, Fig. 15 shows the speed profiles of the motor and of the generator, while Fig. 16 shows the associated powers generated by the stator and absorbed by the rotor. The ohmic losses were subtracted from the rotor power. At the beginning of the experiment, the rotor power is zero, and the generator speed is higher than the motor speed. This difference in speed is needed to compensate for ohmic losses in the generator and would be expected to be smaller in a large machine.

When the motor accelerates, Fig. 16 shows that the rotor supplies a boost of energy taken from the storage. The energy is recovered when the motor decelerates. Alternatively, the second half of the experiment shows what happens when the motor speed stays the same, but the generator speed varies. One finds that energy flows back in the storage when the generator speed increases while the battery is drained when the generator speed decreases. An exact procedure to manage the stored power using the speed of the prime mover is not described in this paper, but could follow the concepts proposed in [30].

V. Future Work

The success obtained in the experiments of this paper provides justification for simulations and experiments at higher power levels. For the propulsion application, the control of two or more motors using a single generator would also be of interest. The problem for two motors connected to a single inverter was considered in [31], and the approach could be extended to the DFIG topology.

Although the prime mover speed was shown to be a possible tool to manage energy storage, the paper left open the design of a high-level control system coordinating the control of the motor speed, the generator speed, the prime mover power, and the stored energy. Such a system would optimize efficiency and ensure the satisfaction of constraints in ways that were not described here. The model predictive control method of [32] and other energy management techniques [30], [33], [34] could be applied towards that objective.

VI. Conclusion

The paper demonstrated how the speed of a PMSM can be controlled through the rotor-side converter of a doubly-fed induction generator. An integrated model of the motor/generator set was developed that accounted for the relationship between the stator voltages and currents of the two machines. Derivations were simplified through the use of complex representations. Control algorithms based on a voltage command mode and a current command mode were proposed. Both versions of the algorithm made it possible to track speed references and recover from a disturbance that caused a loss of synchronism for a synchronous generator. The current command mode provided better speed tracking and faster recovery. By exploiting the characteristics of doubly-fed induction machines, it was shown that strategies could be developed to manage the stored energy of a battery.

The real-life implementation of the proposed configuration requires integrating more system variables like the state of charge and size of the energy storage, generator speed, fuel level, temperature, etc. Different applications require different approaches. For example, the storage capacity for a hybrid aircraft is relatively lower than for an HEV/EV application due to the weight of the battery.

Possible applications of the proposed method include future hybrid-electric aircraft, ships, and large vehicles. The approach offers an alternative option to the conventional motor/generator system using full power converters. Although the solution with a DC bus presents many advantages, the DFIG approach with an AC bus requires the conversion of smaller amounts of power, reducing the converter weight, power losses, and the cooling requirements associated with power electronic converters.

VII. Acknowledgment

The authors thank Ray Beach, Linda Taylor, and David Sadey from the NASA Glenn Research Center for discussions on hybrid-electric propulsion that led to the formulation of the control problem studied in this paper.

References

[1] R. Dyson, “NASA hybrid-electric aircraft propulsion,” *NIEA Biomimicry Summit*, Ohio, Oct. 4, 2017.

[2] C. Pornet, and A. Isikveren, “Conceptual design of hybrid-electric transport aircraft,” *Prog. Aero. Sci.*, vol. 79, 2015, pp. 114–135. DOI: 10.1016/j.paerosci.2015.09.002

[3] N. Bennabi *et al.*, "Hybrid propulsion systems for small ships: context and challenges," *Intl. Conf. Elec. Mach.*, Lausanne, 2016, pp. 2948-2954, DOI: 10.1109/ICELMACH.2016.7732 943.

[4] M. Bodson and M. A. Hossain, "Integrated control of a motor/generator set composed of doubly fed induction machines," in *IEEE J. Emerg. Sel. Top. Pow. Elec.*, vol. 8, no. 2, pp. 1858-1869, June 2020, DOI: 10.1109/JESTPE.2019.2954774.

[5] N. Jackson, “Infographic: how does a hybrid car engine actually work?,” The Atlantic, Jun. 2011. [Online] Available:www.theatlantic.com/technology/archive/2011/06/infographic-how-does-a-hybrid-car-engine-actually-work/241021/

[6] J. Cao, D. Bharathan, and A. Emadi, “Efficiency and loss models for key electronic components of hybrid and plug-in hybrid electric vehicles' Electrical Propulsion Systems,” *IEEE Vehicular Pow. Propul. Conf.*, Arlington, TX, 2007, pp. 477-482.

[7] D. J. Sadey, L. M. Taylor, and R.F. Beach, “Proposal and development of a high voltage variable frequency alternating current power system for hybrid electric aircraft,” *14th Intl. Ener. Conv. Eng. Conf.*, Salt Lake City, UT, July 2016.

[8] M. Hallak, M. Hasni, and M. Menaa, “Modeling and control of a doubly fed induction generator base wind turbine system,” *2018 Intl. Conf. Elec. Sci. Tech. Maghreb*, Algiers, 2018, pp. 1-5.

[9] Q. Gao *et al.*, “Cage rotor structure and its effect on magnetic field modulation of brushless doubly-fed machine,” *2008 Intl. Conf. Elec. Mach. Sys.*, Wuhan, 2008, pp. 4234-4239.

[10] A. M. Knight, R. E. Betz, and D. Dorrell, “Design principles for brushless doubly fed reluctance machines,” *IECON 2011 - 37th An. Conf. IEEE Ind. Elec. Soc.*, Melbourne, VIC, 2011, pp. 3602-3607.

[11] F. Xiong and X. Wang, “Design of a low-harmonic-content wound rotor for the brushless doubly fed generator,” *IEEE Trans. Ener. Conv.*, vol. 29, no. 1, pp. 158-168, March 2014.

[12] F. Zhang *et al.*, “Research of a novel brushless doubly-fed generator with hybrid rotor,” *IEEE Trans. App. Supercond.*, vol. 26, no. 7, pp. 1-5, Oct. 2016.

[13] P. Han, M. Cheng and R. Luo, “Design and analysis of a brushless doubly-fed induction machine with dual-stator structure,” *IEEE Trans. Ener. Conv.*, vol. 31, no. 3, pp. 1132-1141, Sept. 2016.

[14] F. V. Cerna *et al.*, "Efficient automation of an HEV heterogeneous fleet using a two-stage methodology," in *IEEE Trans. Vehicular Tech.*, vol. 68, no. 10, pp. 9494-9506, Oct. 2019, DOI: 10.1109/TVT.2019.2937452.

[15] P. Chakraborty and B. Moulik, "Power management and control of HEV using model predictive control," *Intl. Conf. Sig. Proc. Integ. Net.*, Noida, 2018, pp. 209-214, DOI: 10.1109/SPIN.2018.8474061.

[16] D. Tang *et al.*, "The energy management and optimization strategy for fuel cell hybrid ships," *Intl. Conf. Sys. Rel. Safety*, Milan, 2017, pp. 277-281, DOI: 10.1109/ICSRS.2017.8272834.

[17] A. T. Elsayed and O. A. Mohammed, "A comparative study on the optimal combination of hybrid energy storage system for ship power systems," *IEEE Elec. Ship Tech. Symp.*, Alexandria, VA, 2015, pp. 140-144, DOI: 10.1109/ESTS.2015.7157876.

[18] P. Sumathi and R. Azhagumurugan, "Novel modular multiple input bi-directional DC-DC power converter using fuzzy network for HEV/FCV application," *Intl. Conf. Comp. Pow. Ener. Inf. Comm.* (ICCPEIC), Chennai, 2016, pp. 439-444, DOI: 10.1109/ICCPEIC.2016.7557273.

[19] Y. Song and B. Wang, "Evaluation methodology and control strategies for improving reliability of HEV power electronic system," in *IEEE Trans. Vehicular Tech.*, vol. 63, no. 8, pp. 3661-3676, Oct. 2014, DOI: 10.1109/TVT.2014.2306093.

[20] X. Xu *et al.*, "Modulation and control of an ANPC/H-bridge hybrid inverter for ship electric propulsion drives," *Intl. Conf. Elec. Mach. Sys.*, Harbin, China, 2019, pp. 1-5, DOI: 10.1109/ICEMS.2019.8922323.

[21] W. Long *et al.*, "Symmetrical hybrid multilevel inverters for ship electric propulsion drives," *IEEE 4th Intl. Future Ener. Elec. Conf.*, Singapore, Singapore, 2019, pp. 1-6, DOI: 10.1109/IFEEC47410.2019.9015090.

[22] P. Han, M. Cheng and R. Luo, “Design and analysis of a brushless doubly-fed induction machine with dual-stator structure,” *IEEE Trans. Ener. Conv.*, vol. 31, no. 3, pp. 1132-1141, Sept. 2016.

[23] P. Pisek *et al.*, "Design analysis and experimental validation of a double rotor synchronous PM machine used for HEV," in *IEEE Trans. Mag.*, vol. 49, no. 1, pp. 152-155, Jan. 2013, DOI: 10.1109/TMAG.2012.2220338.

[24] A. Gohardani, G. Doulgeris, and R. Singh, “Challenges of future aircraft propulsion: a review of distributed propulsion technology and its potential application for the all electric commercial aircraft,” *Prog. Aero. Sci.*, vol. 47, 2011, pp. 369–391. DOI:10.1016/j.paerosci.2010.09.001

[25] K. Reynolds *et al.*, “Wing shaping concepts using distributed propulsion,” *Air. Eng. Aero. Tech.*, vol. 86, no. 6, 2014, pp. 478–482. DOI:10.1108/AEAT-04-2014-0050

[26] R. S. Munoz-Aguilar, A. Doria-Cerezo and P. F. Puleston, "Energy-based modelling and simulation of a series hybrid electric vehicle propulsion system," *2009 13th Euro. Conf. Pow. Elec. App.*, Barcelona, 2009, pp. 1-10.

[27] M. Bodson, “Speed control for doubly fed induction motors with and without current feedback,” *IEEE Trans. Cont. Sys Tech.*, vol. 28, no. 3, pp. 898-907, May 2020.

[28] S.-K. Sul, “Control of electric machine drive systems,” Wiley, Hoboken, NJ, 2011.

[29] R. Ortega *et al.*, “Two provably stable observers for rotor position and speed of permanent magnet synchronous motors,” LSS, Gif-sur-Yvette Cedex, France, Int. Report LSS, Jan. 2009.

[30] L. Gomez *et al.*, “Combined control of DFIG-based wind turbine and battery energy storage system for frequency response in microgrids,” *Energies*, v. 13, n. 4, p. 894, 2020.

[31] T. Liu and M. Fadel, “An efficiency-optimal control method for mono-inverter dual-PMSM systems,” *IEEE Trans. Ind. App.*, vol. 54, no. 2, pp. 1737-1745, March-April 2018.

[32] J. Hou, J. Sun and H. Hofmann, “Integrated control of power generation, electric motor and hybrid energy storage for all-electric ships,” *2016 Amer. Cont. Conf.*, Boston, MA, 2016, pp. 6797-6802.

[33] S. Faddel *et. al*, “Decentralized control algorithm for the hybrid energy storage of shipboard power system,” *IEEE J. Emer. Sel. Top. Pow. Elec.*, vol. 8, no. 1, pp. 720-731, March 2020.

[34] M. M. S. Khan and M. O. Faruque, “Energy storage management for MVDC power system of all electric ship under different load conditions,” *2017 IEEE Elec. Ship Tech. Symp.*, Arlington, VA, 2017, pp. 192-199.